

Structural organization of the dynein–dynactin complex bound to microtubules

Saikat Chowdhury¹, Stephanie A Ketcham², Trina A Schroer^{2,3} & Gabriel C Lander^{1,3}

Cytoplasmic dynein associates with dynactin to drive cargo movement on microtubules, but the structure of the dynein–dynactin complex is unknown. Using electron microscopy, we determined the organization of native bovine dynein, dynactin and the dynein–dynactin–microtubule quaternary complex. In the microtubule-bound complex, the dynein motor domains are positioned for processive unidirectional movement, and the cargo-binding domains of both dynein and dynactin are accessible.

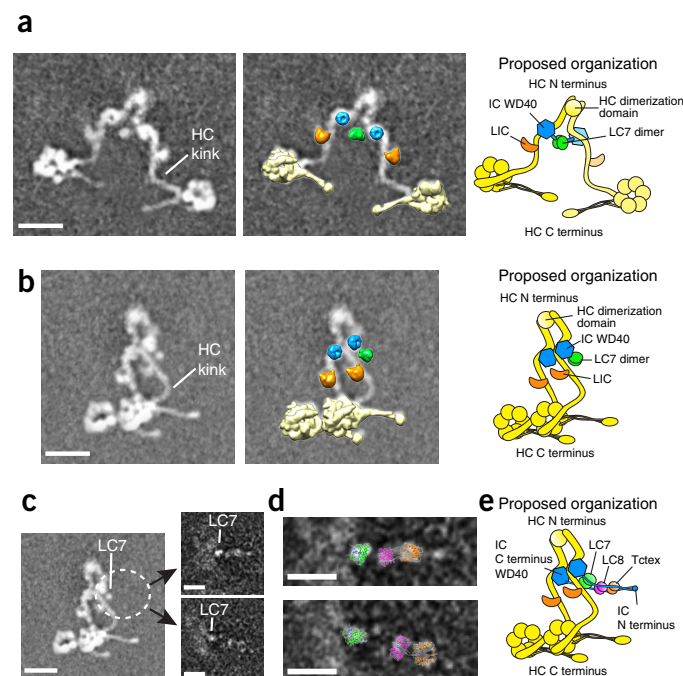
Cytoplasmic dynein-1 (hereafter dynein) interacts with its cofactor dynactin to transport a variety of cellular cargos toward microtubule (MT) minus ends, supporting events critical for cell division and survival¹. Although the structure and the mechanical behavior of simplified versions of dynein's catalytic motor domain have been elucidated^{2,3}, the mechanism by which the dimeric dynein holoenzyme powers movement of intracellular cargos over long distances has remained undefined, primarily owing to a lack of structural information for the dynein–dynactin–MT complex.

Dynein is a dimeric multisubunit complex comprising a pair of ~500-kDa heavy chains (HCs) that contain the motor domain. Each HC also binds a light intermediate chain (LIC) and an intermediate chain (IC) that is complexed with three light chains (LCs; LC7, LC8 and Tctex); together, these components form the tail domain that binds cargo⁴. We performed negative-stain EM studies of vertebrate dynein, which can

be observed as V-shaped dimers (Supplementary Fig. 1). Traditional two-dimensional (2D) analysis of whole particles yielded averages with limited resolvable structural detail (Supplementary Fig. 1b), owing to the extreme conformational flexibility of the head–tail link^{5–7}. To overcome this challenge, we developed a ‘divide and conquer’ image-processing approach (Online Methods and Supplementary Fig. 2a) to reveal the organization of the dynein holoenzyme in unprecedented detail.

In the class averages, two tail-dimerization sites are visible: one at the distal end of the tail and a second positioned about 13 nm closer to the motor domains. The distal mass has long been ascribed to the three LCs⁸. The second mass, which to our knowledge has never been described, is positioned between donut-shaped lobes (Fig. 1) corresponding to the IC β -propeller domains⁹. The organization of the three LCs on the IC polypeptide has been established biochemically¹⁰, and the proximity of this second dimerization density to the WD40 domains suggests that it corresponds to the LC7 dimer (Fig. 1). Focused 2D analysis of the region extending beyond the putative LC7 dimer shows two

Figure 1 Proposed architecture of native vertebrate cytoplasmic dynein. (a,b) Left, negative-stain class averages of the purified dynein dimer. Middle, atomic coordinates for known dynein subunits (yellow, head domain, PDB 3VKH; orange, LIC, PDB 3W7G; green, LC7, PDB 3L9K) and a seven-bladed β -propeller (blue), filtered to simulate low-resolution EM density and overlaid on the class averages. Right, cartoon representations of the proposed subunit architecture in the class averages. The locations of the HC dimerization domain and IC WD40 domain were recently established¹¹. (c) IC-associated densities, identified through focused 2D analysis of the region surrounding the putative LC7-dimer density (white dashed circle). Densities proposed to correspond to the LC8 and Tctex dimers project away from the LC7 dimer at a range of orientations relative to the dynein tail (shown on right) and do not appear to make any contact with the HC. (d) Crystal structures for LC7 (green, PDB 3L9K), LC8 and Tctex (magenta and orange, respectively, PDB 2PG1), superimposed on the 2D averages in c. (e) Cartoon representation of the proposed organization of dynein subunits. Scale bars, 10 nm.



¹Department of Integrative Structural and Computational Biology, Scripps Research Institute, La Jolla, California, USA. ²Department of Biology, Johns Hopkins University, Baltimore, Maryland, USA. ³These authors jointly supervised this work. Correspondence should be addressed to G.C.L. (glander@scripps.edu).

Received 7 February; accepted 2 March; published online 9 March 2015; doi:10.1038/nsmb.2996

densities that probably correspond to the LC8 and Tctex dimers that bind the IC N terminus. This mobile IC-LC domain does not appear to interact with any portion of the HC. These data lead to a new refined model of dynein tail organization in which the distal portion comprises exclusively the HC, in agreement with a recent report¹¹.

Beyond the IC WD40 domains, a small crescent-shaped density is bound to each HC. We attribute these to the LICs, which bind to residues 650–800 of the HC¹², between the IC-binding site and motor domain. Beyond the LIC, the HC exhibits a dramatic kink that has not been observed in previous studies^{5–7,13}. The function of the kink, which we observed in 100% of the dynein averages (**Supplementary Fig. 2b**), is unclear, but its location between the tail and heads suggests that it may serve as a hinge that allows motions associated with the mechanochemical cycle of the head to occur without disrupting tail-cofactor-cargo interactions¹⁴.

Dynein-based movement of cellular cargos depends upon dynactin, a multiprotein assembly containing distinct domains that bind dynein, MTs and cargos¹⁵. The dynactin assembly consists of an actin-like polymer of the actin-related protein Arp1, with distinct protein complexes attached at either end¹⁶. A large structure ('shoulder') containing a dimeric assembly of p24, p50 and p150^{Glued} projects from the side of the Arp filament near its barbed end. The pointed end of the Arp filament binds a complex of Arp11, p62, p27 and p25, subunits that contribute to dynactin-complex stability and cargo binding^{17,18}. Although models, based on biochemical analysis and low-resolution EM^{19,20}, exist for dynactin subunit organization, the detailed architecture of this complex has only recently been described¹¹.

We determined the structure of native dynactin purified from bovine brain as previously described⁴, resolving the Arp filament to 6.5 Å by cryo-EM. Because the shoulder readily detaches during vitrification, it is not present in the reconstruction. We determined the organization of the entire vertebrate dynactin complex by fitting the 6.5-Å cryo-EM structure of the filament into a 24-Å-resolution negative-stain structure of the intact complex (**Fig. 2** and **Supplementary Figs. 3** and **4**). The two-stranded helical organization of the Arp polymer (four copies in one strand, five in the other) is obvious in the structures (**Fig. 2a**). Dynactin's single actin protomer¹⁵ lies at the pointed end of the four-strand polymer¹¹. At the barbed end of the filament, helices corresponding to the α - and β -tentacles of CapZ- α and CapZ- β are seen bound to the first Arp1 in each filament strand (**Supplementary Fig. 4c**). Arp11 contacts protomers of both filament strands at the opposite end. The remainder of the pointed-end domain is not as well resolved, owing to intrinsic flexibility, but densities corresponding to the p25 and p27 subunits are discernible as two paralleloid prisms (**Fig. 2b**). The remaining unaccounted density, which lies between Arp11 and the p25–p27 dimer, is attributed to the p62 subunit.

The p150^{Glued} dimer, a component of the shoulder, contains an N-terminal coiled-coil domain that is absent in the three-dimensional (3D) reconstruction, owing to its flexibility. Focused 2D analysis of the shoulder region reveals a mobile coiled-coil extension with a globular density at its end (**Supplementary Fig. 3c**). The globular structure that we observe is much larger than what would be expected for the MT-binding CAP-Gly domain located at the p150^{Glued} N terminus¹⁵.

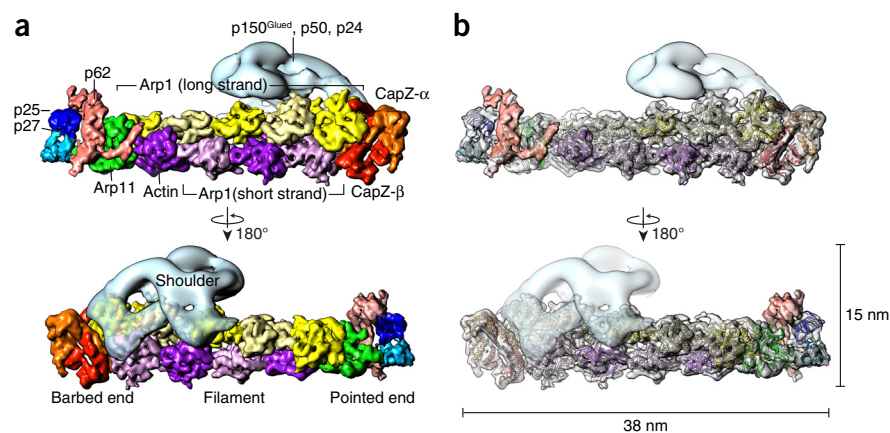


Figure 2 Subunit organization of vertebrate dynactin. (a) The 6.5-Å-resolution cryo-EM structure of the dynactin filament including the barbed-end and pointed-end complexes (solid surface representation), combined with a 24-Å-resolution negative-stain structure of the shoulder domain (transparent surface representation, light blue). Each subunit of dynactin is colored individually. The Arp filament contains a long strand (five subunits, yellow and light yellow) and a short strand (four subunits, purple and light purple). The protomer at the pointed end of the short strand is actin¹¹; all others are Arp1. The CapZ heterodimer (orange and red) caps the filament at the barbed end, and the pointed-end complex (Arp11, p62, p27 and p25) caps the filament at the pointed end. (b) Atomic model for CapZ (PDB 1IZN), homology models for Arp1 and Arp11, and two copies of p27 (PDB 3TV0) fit into the cryo-EM density.

Furthermore, the position of the density 20 nm from the shoulder is incompatible with the predicted 50-nm length of the p150^{Glued} coiled coil. This domain probably corresponds to the recently described p150^{Glued} ~40-kDa intercoil domain¹¹. The globular density may contribute to dynactin regulation in heretofore-undefined ways, perhaps by governing the mobility of the coiled-coil region to accommodate and facilitate simultaneous interactions of dynactin with both MTs and dynein.

Vertebrate dynein is not processive in the absence of dynactin but instead undergoes diffusive bidirectional movement²¹. Dynactin binding converts this behavior into longer-range, unidirectional motion²², particularly when the N-terminal fragment of cofactor bicaudal D homolog 2 (BicD2N) is added^{13,21}. Attempts by other groups to determine the structural arrangement of the dynein–dynactin–BicD2N (DDB) complex were inconclusive, presumably owing to the conformational heterogeneity of dynein^{13,21}.

Because MT binding is expected to limit the conformational flexibility of dynein and the DDB complex, we prepared native dynein–dynactin complexes stabilized with BicD2N and bound to MTs (DDB–MT) (**Supplementary Fig. 5a,b**). In negative-stain micrographs, the DDB complexes are discernible as structures of ~45 nm in length, attached at a range of angles to the MT surface but tilted in a single direction, consistently with directional movement (**Supplementary Fig. 5c**). We produced detailed class averages of the DDB–MT complex with the same focused classification strategy used for dynein (**Supplementary Fig. 5d,e**).

In the DDB–MT complex, dynein is aligned between dynactin and the MT with the distal part of the dynein tail near the dynactin pointed end. The dynein tail associates with the short strand of the dynactin Arp filament, on the side opposite the shoulder (**Fig. 3**), consistently with the recently determined structure of the isolated dynein tail–dynactin–BicD2N complex¹¹. Densities that cannot be attributed to either dynactin or dynein probably correspond to the BicD2N coiled coil. Notably, the centers of the dynein heads are ~17 nm away from the MT, and the MT-binding stalks are oriented at an acute angle (**Supplementary Fig. 5d,e**). Unlike the motor domains in free DDB complexes^{13,21}, which exhibit a range of orientations and separation,

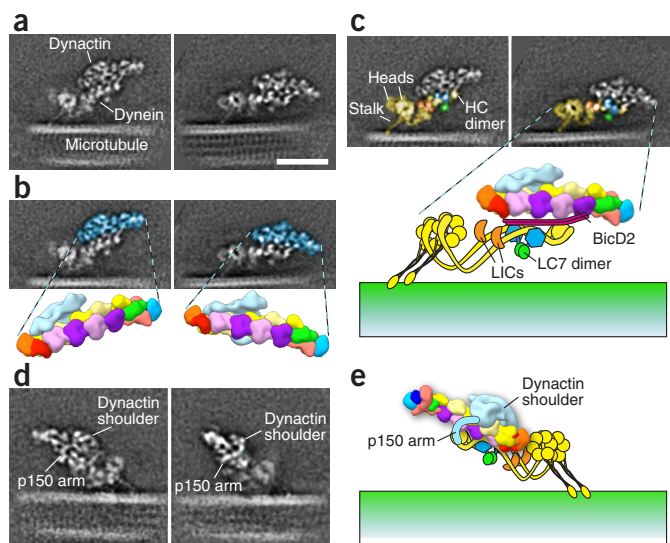


Figure 3 Organization of the DDB–MT complex. **(a)** Two class averages of MT-bound DDB complexes, attached at slightly different angles relative to the MT. **(b)** Top, same class averages as in **a**, with dynactin colored blue. Bottom, low pass-filtered 3D model (colored as in **Fig. 2a**), oriented to correspond to the class average. **(c)** Dynein components in the 2D averages, assigned on the basis of information determined from the isolated-dynein class averages. Yellow, HCs; orange, LICs; blue, IC C-terminal WD40 domain; green, putative LC7 dimer. **(d)** Two class averages of DDB–MT complexes, showing the location of the shoulder and an extension (p150 arm) that wraps around the Arp1 filament and contacts dynein. We propose that this corresponds to the p150^{Glued} coiled coil. **(e)** A model of the DDB complex in the same orientation as the averages in **d**, with the path of the putative p150^{Glued} coiled-coil extension (p150 arm) traced in light blue. Scale bar in **a**, 25 nm; all EM images are at the same scale.

METHODS

Methods and any associated references are available in the [online version of the paper](#).

Accession codes. Density maps of the negative-stain and cryo-EM dynein reconstructions have been deposited in the Electron Microscopy Data Bank under accession codes EMD-6290 and EMD-6289, respectively.

Note: Any Supplementary Information and Source Data files are available in the online version of the paper.

ACKNOWLEDGMENTS

We thank R. McKenney (R. Vale laboratory, University of California, San Francisco) for providing the BicD2N construct, and the S. Encalada laboratory (Scripps) for providing mouse brains. We are enormously grateful to R. Milligan for his ongoing support and input into this project. This work was supported by the Damon Runyon Cancer Research Foundation (DFS-#07-13), the Pew Scholars program, the Searle Scholars program, and US National Institutes of Health (NIH) grant DP2 EB020402-01 to G.C.L. and NIH grant GM44589 to T.A.S.

AUTHOR CONTRIBUTIONS

S.A.K. prepared the isolated dynein and dynactin. S.C. prepared the MT–DDB complex and performed all electron microscopy, image analysis and reconstructions. All authors contributed to the experimental design and assembly of the manuscript.

COMPETING FINANCIAL INTERESTS

The authors declare no competing financial interests.

Reprints and permissions information is available online at <http://www.nature.com/reprints/index.html>.

those in DDB–MT complexes are in proximity to each other (about 7 nm apart) but are not locked into a single orientation relative to each other (**Supplementary Fig. 5e–g**). The adjacent HC kink may provide a flexible ‘shock absorber’ that allows the motor domains to undergo the structural changes that underlie stepping without interfering with dynactin and cargo interactions. The organization of dynein and dynactin in the DDB–MT complex also elucidates the arrangement of cargo-binding domains. Using the isolated-dynein class averages for comparison, we found that densities corresponding to the IC–LC dimerization domain and the LICs (**Fig. 3c**) are apparently exposed in the DDB–MT complex. Given the importance of these regions for interactions with dynactin and other binding partners, it makes sense that these parts of the tail remain accessible.

The dynactin shoulder position on the opposite side of the DDB complex from the MT is intriguing, given that the projecting p150^{Glued} arm contains a MT-interacting domain. Although we did not observe a MT-associated density that might correspond to this domain, we observed a thin filamentous extension emerging from the shoulder in certain averages (**Fig. 3d**). The extension curves around the dynactin Arp filament and appears to make contact with the IC dimerization domain but cannot be traced further. We propose that this extension is the C-terminal portion of the p150^{Glued} coiled coil, which may engage with dynein to help secure it to dynactin during processive movement (**Fig. 3e**).

This analysis provides the first visualization, to our knowledge, of the dynein–dynactin complex bound to microtubules, revealing an organization in which the HCs are oriented with the motor domains aligned to favor unidirectional movement. At the same time, the complex is structured in a way that favors cargo recruitment (**Fig. 3c**). The insights provided here will serve as a paradigm for understanding the dynein–dynactin interactions that are essential for a wide range of minus end–directed motile phenomena. Although more detailed structural information will certainly improve understanding of the mechanism of dynein–dynactin–dependent movement, high-resolution determination of this entire structure will be extremely challenging because of the large size of the DDB complex and the heterogeneity of its link to the MT surface. The organizational framework of the DDB complex presented here provides the foundation for future work, supplying a new structural context for interpreting decades of biophysical and biochemical studies aimed at deciphering the mechanics of this fundamental and ancient cellular transport system.

- Kardon, J.R. & Vale, R.D. *Nat. Rev. Mol. Cell Biol.* **10**, 854–865 (2009).
- Carter, A.P. *J. Cell Sci.* **126**, 705–713 (2013).
- Roberts, A.J., Kon, T., Knight, P.J., Sutoh, K. & Burgess, S.A. *Nat. Rev. Mol. Cell Biol.* **14**, 713–726 (2013).
- Bingham, J.B., King, S.J. & Schroer, T.A. *Methods Enzymol.* **298**, 171–184 (1998).
- Vallee, R.B., Wall, J.S., Paschal, B.M. & Shpetner, H.S. *Nature* **332**, 561–563 (1988).
- Amos, L.A. *J. Cell Sci.* **93**, 19–28 (1989).
- Steffen, W., Hodgkinson, J.L. & Wiche, G. *J. Struct. Biol.* **117**, 227–235 (1996).
- Vale, R.D. *Cell* **112**, 467–480 (2003).
- Wilkerson, C.G., King, S.M., Koutoulis, A., Pazour, G.J. & Witman, G.B. *J. Cell Biol.* **129**, 169–178 (1995).
- Hall, J., Song, Y., Karplus, P.A. & Barbar, E. *J. Biol. Chem.* **285**, 22566–22575 (2010).
- Urnavicius, L. *et al. Science* doi: 10.1126/science.aaa4080 (12 February 2015).
- Tynan, S.H., Gee, M.A. & Vallee, R.B. *J. Biol. Chem.* **275**, 32769–32774 (2000).
- Schlager, M.A., Hoang, H.T., Urnavicius, L., Bullock, S.L. & Carter, A.P. *EMBO J.* **33**, 1855–1868 (2014).
- Burgess, S.A., Walker, M.L., Sakakibara, H., Oiwa, K. & Knight, P.J. *J. Struct. Biol.* **146**, 205–216 (2004).
- Schroer, T.A. *Annu. Rev. Cell Dev. Biol.* **20**, 759–779 (2004).
- Eckley, D.M. *et al. J. Cell Biol.* **147**, 307–320 (1999).
- Yeh, T.Y. *et al. EMBO J.* **32**, 1023–1035 (2013).
- Yeh, T.Y., Quintyne, N.J., Scipioni, B.R., Eckley, D.M. & Schroer, T.A. *Mol. Biol. Cell* **23**, 3827–3837 (2012).
- Hodgkinson, J.L., Peters, C., Kuznetsov, S.A. & Steffen, W. *Proc. Natl. Acad. Sci. USA* **102**, 3667–3672 (2005).
- Imai, H., Narita, A., Maeda, Y. & Schroer, T.A. *J. Mol. Biol.* **426**, 3262–3271 (2014).
- McKenney, R.J., Huynh, W., Tanenbaum, M.E., Bhabha, G. & Vale, R.D. *Science* **345**, 337–341 (2014).
- King, S.J. & Schroer, T.A. *Nat. Cell Biol.* **2**, 20–24 (2000).

ONLINE METHODS

Purification of dynein and dynactin, and analysis of MT binding. Dynein and dynactin were purified from bovine brain (purchased from a local butcher) by a combination of sucrose-gradient centrifugation and ion-exchange chromatography, as described in ref. 23 but with the following changes. Dynein and dynactin were eluted from a MonoQ 10/100 column with a linear salt gradient. Then each pool (identified by SDS-PAGE) was rechromatographed separately on a MonoQ 5/50 column and eluted with a salt bump. Between 2 and 5 ml of the peak dynein and dynactin fractions was supplemented with 1 mM TCEP and microconcentrated (without desalting or dilution) to ≈ 0.5 ml to yield a final concentration of 1–3 mg/ml. Proteins were kept on ice until use. The appearance of these complexes in negative-stain EM was indistinguishable from that of those isolated with AMP-PNP–MT binding from chick embryo brain, as described previously²⁴. AMP-PNP-dependent binding of bovine dynein to MTs (**Supplementary Fig. 5a**) was analyzed with a method described previously²⁴, except purified dynein was used, and nucleotide conditions in the MT-copelleting step were varied.

Expression and purification of BicD2N. A plasmid encoding mouse BicD2 aa 25–400 (BicD2Nsh; hereafter BicD2N) in pET28a (kanamycin resistant) with an N-terminal His₆ and StrepII-superfold GFP tag²¹ (generously provided by R. McKenney) was transformed into BL21(DE3) cells containing a pACYC-Duet-1 (chloramphenicol resistance) plasmid with rare tRNAs for codon usage in *Escherichia coli*. Cells were then grown at 30 °C in 2× LB medium²⁵ containing 35 µg/ml chloramphenicol and 50 µg/ml kanamycin until cell density reached OD_{600nm} ≈ 0.4 . The temperature was then dropped to 18 °C, and cultures were induced with 1 mM IPTG (Sigma Aldrich). Cells were grown overnight at 18 °C and harvested, and the cell pellet was flash frozen in liquid nitrogen and stored at –80 °C for later purification.

The frozen cell pellet was thawed on ice and resuspended in lysis buffer containing 50 mM NaH₂PO₄, pH 8.0, 300 mM NaCl, 10 mM imidazole, and 1× EDTA-free protease inhibitor (G Biosciences). After the cells were lysed by ultrasonication, the lysate was cleared of insoluble cell debris by centrifugation at 35,000g for 45 min, passed through a 0.2-µm syringe filter and incubated with HisPur Ni-NTA resin (Fisher Scientific) for 2 h at 4 °C. The Ni resin was washed extensively with 50 mM NaH₂PO₄, pH 8.0, 300 mM NaCl, and 20 mM imidazole, and BicD2N was eluted with the same buffer containing 250 mM imidazole. The His tag-purified BicD2N was concentrated and passed over a Superose 6 gel-filtration column (GE Healthcare) equilibrated with 50 mM NaH₂PO₄, pH 8.0, 300 mM NaCl and 1 mM TCEP. Pure BicD2N fractions identified by SDS-PAGE were pooled, and glycerol was added to a final concentration of 5% (w/v). The pooled fractions were then concentrated to 18 µM, flash frozen in liquid nitrogen and stored at –80 °C for later use.

Purification of dynein–dynactin–BicD2N complex bound to MT from mouse brain. 5 g of fresh brain tissue from a 3-month-old female C57BL/6J mouse was washed with ice-cold PMEE buffer (35 mM PIPES, pH 7.2, 5 mM MgSO₄, 1 mM EGTA, 0.5 mM EDTA, and 6.8% (w/v) glycerol) supplemented with 1× protease inhibitor and 1 mM TCEP, then homogenized in an ice-cold Dounce homogenizer. The homogenate was centrifuged at 36,000g for 15 min at 2 °C, and the supernatant was centrifuged at 90,000g for 30 min at 2 °C. BicD2N was added to the final supernatant at 500 nM, and the mixture was incubated on ice for 2 h with gentle swirling every 20 min to mix. 4 mM MgSO₄, 1 mM GTP (Sigma-Aldrich) and 4 mM AMP-PNP (Sigma-Aldrich) were added, and the mixture was incubated for 10 min at 37 °C. AMP-PNP was used to promote tight binding of the dynein motor to the MT surface (**Supplementary Fig. 5a**). The mixture was supplemented with 20 µM taxol (Cytoskeleton, Inc.) and further incubated for 15 min at 37 °C. The polymerized MTs, along with bound DDB particles, were pelleted by centrifugation at 21,000g for 30 min at 30 °C. The pellet was washed by resuspension in PMEE buffer containing 4 mM MgSO₄, 1 mM GTP, 4 mM AMP-PNP and 20 µM taxol, and the MTs were pelleted as above. The final pellet was resuspended in ten times its volume of PMEE buffer containing 4 mM MgSO₄, 1 mM GTP, 4 mM AMP-PNP and 20 µM taxol at room temperature. The presence of DDB–MT complexes in the suspension was confirmed by SDS-PAGE and negative-stain EM (**Supplementary Fig. 5b,c**). The protocol for this work was reviewed and approved by the TSRI IACUC office under protocol 14-0013.

Sample preparation for negative-stain EM analysis. Grids for negative-stain analysis of isolated dynein or dynactin were prepared in a similar fashion. Dynein

and dynactin samples were diluted to 20 and 50 µg/ml, respectively, in a buffer containing 35 mM Tris, pH 7.2, 5 mM MgSO₄, 150 mM KCl and 1 mM TCEP. A 4-µl aliquot was applied to freshly cleaned 400-mesh Cu-Rh maxtaform grids (Electron Microscopy Sciences) that had been coated with a thin layer of carbon. After incubation for 1 min, excess protein was wicked off with a piece of filter paper, and the grid was immediately inverted and placed on a 50-µl droplet of 2% (w/v) uranyl formate solution. After 30 s, excess stain was wicked off from the grid by touching the edge with filter paper. This staining step was repeated three times for thorough embedding of the sample, and the grids were air dried after the last blotting step.

In the case of isolated dynactin, a majority of the particles exhibited a preferential orientation on the carbon support. To overcome this issue, we pretreated the plasma-cleaned carbon surface on grids with 5 µl of 0.1% (w/v) poly-L-lysine hydrobromide (Polysciences) for 90 s; this was followed by two washes with 10-µl drops of water. After the grids dried, the dynactin sample was applied and stained as described above. This treatment enabled us to obtain several additional views of dynactin that were missing earlier without this pretreatment.

A similar staining strategy was used to prepare grids for analysis of the MT–DDB complex. The final MT–DDB suspension was diluted 15-fold in PMEE buffer supplemented with 4 mM MgSO₄, 1 mM GTP, 4 mM AMP-PNP, and 20 µM taxol. The staining steps were performed in the same fashion as for the isolated dynein complex.

Sample preparation for cryo-EM analysis. Purified dynactin was applied to freshly glow-discharged 400-mesh C-Flat grids (Protochips) containing 2-µm-diameter holes spaced 2 µm apart. Immediately before application of protein sample on the grid, 0.025% (w/v) amphipol A8-35 (Anatrace) was mixed with the sample to aid in dispersing dynactin particles across the holes in the carbon. 4 µl of the dynactin sample was applied to the grid, excess sample was manually blotted with filter paper for ~ 5 –7 s, and the sample was immediately vitrified by plunge freezing in liquid-ethane slurry at –179 °C. The entire procedure was carried out at 4 °C and 98% humidity.

Data acquisition. All negative-stain and cryo-EM data were acquired with the Leginon automated data acquisition system²⁶. Data acquisition for negative-stained samples was performed on a Tecnai Spirit (FEI) transmission electron microscope operating at 120 keV. Images were collected at a nominal magnification of 52,000× on an F416 CMOS 4K × 4K camera (TVIPS) with a pixel size of 2.05 Å/pixel at specimen level. All micrographs were collected with an electron dose of 20 electrons/Å² with a defocus range from 0.3 µm to 1.5 µm.

Cryo-EM data for dynactin were collected on a Titan Krios (FEI) transmission electron microscope operating at 300 keV, with a Gatan K2 Summit camera operated in counting mode at a dose rate of ~ 10 electrons/pixel/s. Each movie comprised 30 frames acquired over 6 s, with a cumulative dose of ~ 35 electrons/Å². Imaging was performed at a nominal magnification of 22,500×, with a pixel size of 1.31 Å/pixel at specimen level with a defocus ranging from 0.8 µm to 4 µm.

Dynein image processing. 1,200 micrographs of negatively stained dynein samples were collected for 2D analysis (**Supplementary Fig. 1**). All image preprocessing and initial 2D analysis were performed with the Appion image-processing pipeline²⁷. The contrast transfer function (CTF) of each micrograph was estimated with CTFindv3 (ref. 28), and template-based automated particle selection was performed with FindEM²⁹. Templates for particle selection were generated from 2D class averages from a small set of manually picked particles. Phases for each micrograph were corrected with EMAN³⁰, and particles were extracted with a 640 pixel × 640 pixel box. The data were binned by a factor of 2 for faster computation. Individual particles were normalized by elimination of pixels with values above or below 4.5σ of the mean pixel value with the normalization function in the XMIPP package³¹.

An initial stack of 120,000 particles was subjected to five rounds of iterative multivariate statistical analysis (MSA)³² and multireference alignment (MRA) in Appion to remove any nonparticle features and aggregates that were erroneously picked by automated particle picker. To speed up this process, the particle stack was further binned by a factor of 4 before analysis. Particles belonging to classes that represented nonparticles or aggregates were eliminated, thus resulting in a stack of 100,000 dynein particles. This particle stack was subjected to one generation of reference-free 2D alignment and classification with ISAC³³, a module in

the EMAN2/SPARX package^{34,35}, after application of a low-pass and high-pass filter of 15 Å and 650 Å, respectively. The stable averages obtained from ISAC had the overall V-shaped feature of dynein with two circular features at the two free ends (**Supplementary Fig. 1b**). Owing to the conformational heterogeneity of dynein, the class averages lacked structural details. In order to improve the resolvable details, we focused on subregions of the molecule (**Supplementary Fig. 2**). For a given class average, soft-edged masks were created to isolate the tail and individual head domains. These masks were applied to the hundreds of aligned particles belonging to the class average. This resulted in three stacks: one with only the tail region visible, another containing the first head domain, and another containing the second head domain. Each group of particles was individually subjected to three generations of reference-free classification and alignment with ISAC, with pixel error values between 3 and 8 and particles per group ranging from 250 to 100 for different generations. The stable averages obtained from these classifications showed markedly improved structural detail.

In order to generate a representative average of the full dynein molecule, the classification and alignment parameters for each individual classification were applied to the unmasked stack of particles. Although the details outside of the focused region of interest were not well resolved after unmasking, structural features such as the kinked HC domain were discernible in many of the tail- and head-domain averages. These common structural features were used to overlay the head and tail classes in order to reassemble a composite view of the entire dynein molecule. For each set of class averages, the kinked region of one of the head domains was positioned in the center of the image, and the kinked region in the corresponding arm of the tail was also positioned in the center. A rotational and translational search with a limited search radius was used to align the kinked region in both class averages, and the averages were then themselves averaged together. This process was repeated for the second head and tail arm, to result in a composite class average of the complete dynein molecule. These class averages not only revealed detailed structural features of dynein but also showed the wide range of conformational heterogeneity of this complex in solution.

A similar masking approach was used to identify the dynein LCs. The unmasked dynein-tail averages (**Supplementary Fig. 2a**) in which the LC7 dimer was clearly visible were selected, and a soft mask was applied to the aligned particles around the area next to and including the LC7 dimer (dotted circle in **Fig. 1b**). These masked particles were subjected to ISAC 2D alignment and classification, and the resulting class averages were unmasked as described earlier.

Dynactin image processing. Preprocessing and initial 2D analysis of the negative-stain dynactin data set were performed in the same manner as described for dynein. From 1,978 micrographs, 88,434 automatically selected particles were extracted with a box size of 480 pixels. After several iterations of particle cleaning by MSA/MRA 2D classification, we obtained 46,734 dynactin particles that included the shoulder domain, which were used for 3D reconstruction. We used a 60-Å low pass-filtered negative-stain reconstruction of dynactin (EMD-2716)²⁰ as our initial model for 3D refinement by iterative projection matching with EMAN2 and SPARX libraries^{34,35}. Refinement of the initial model began generating forward projections at an angular increment of 20°, which decreased incrementally to 1°. The refinement would not proceed to the next angular step size until 95% of the particles had converged to a pixel error of less than 1 pixel. Forward projections of the refined volume showed excellent correlation with reference-free class averages, thus supporting the quality of reconstruction, free from model bias (**Supplementary Fig. 3d**). The resolution of the reconstruction was estimated by splitting the particle stack into odd and even halves and calculating the Fourier shell correlation (FSC) between the resulting volumes. The estimated resolution of the reconstruction at 0.5 FSC was 24 Å (**Supplementary Fig. 3e**).

Owing to its flexibility, the p150^{Glued} coiled-coil arm was not resolved in the 2D averages or 3D reconstructions of the dynactin complex. With a soft mask to perform focused analysis on the region surrounding the shoulder domain, we were able to visualize the p150^{Glued} side arm. A thin filament could be seen extending away from the shoulder domain with a large globular density at the end, ~20 nm from the shoulder. The class averages show that this domain can undergo a wide range of motion (**Supplementary Fig. 3b**).

A total of 2,421 cryo-EM images of dynactin were collected and analyzed for a higher-resolution structure. K2 movie frames were aligned with the GPU frame-alignment program described by Li *et al.*³⁶, which is incorporated into the Appion pipeline. A frame offset of 5 and *B* factor of 1,000 pixels (ref. 2) were used

for the frame-alignment step. CTF parameters were estimated with CTFFindv3, and images reporting a confidence value of less than 90% were discarded. Particles were picked with an automated template picker, as described earlier for negatively stained dynactin data. 133,558 particles were extracted from the aligned micrographs with a box size of 512 pixels, which were binned by a factor of 2 for subsequent processing. As described previously, MSA/MRA 2D classification was used to discard false or damaged particles. The shoulder domain, which we have observed to readily dissociate from the dynactin complex, was absent in almost all the particles in the cryo-EM data set.

After removal of junk particles, a stack of 59,538 particles remained, whose coordinates were imported into Relion³⁷ for 3D classification and reconstruction. Particles were extracted with a box size of 512 pixels and scaled to 256 pixels, with 2.62 Å/pixel values, in order to reduce computational demand. 3D classification into three classes was performed, with the 24-Å negative-stain reconstruction of dynactin filtered to 60 Å as an initial model. After 25 iterations of 3D classification, 33,305 particles belonging to the most well resolved class average were used for further refinement. Refinement by projection matching in Relion resulted in a 9.5-Å-resolution reconstruction of dynactin (by gold-standard FSC at a cutoff of 0.143), although the pointed end was not resolved at subnanometer resolution, owing to the intrinsic flexibility of this region. A soft 3D mask was generated from the 9.5-Å-resolution dynactin reconstruction, and the pointed end of the complex was removed from the mask. Applying this mask during the refinement improved the alignment of the particles and accordingly improved the resolution of the 3D reconstruction to 7.5 Å (by gold-standard FSC at 0.143). The particle-polishing methodology in Relion was then used to improve the resolution of this map to 6.5 Å. The local resolution map shown in **Supplementary Figure 4d** was calculated from the half volumes with the 'bloccs' function in the Bsoft package³⁸.

The individual components that make up the Arp filament of dynactin were clearly discernible, and the map was segmented with the volume-tracer tool in UCSF Chimera³⁹. The cryo-EM reconstruction of the Arp filament could be fit with high precision into the 24-Å-resolution negative-stain dynactin reconstruction. By low-pass filtering of the cryo-EM reconstruction to a comparable resolution and with 'diffmap' from the N. Grigorieff laboratory (<http://grigoriefflab.janelia.org/diffmap/>), it was possible to isolate density for the shoulder domain from the negative-stain structure.

Nine copies of a homology model of Arp1, based on an F-actin as a template (as obtained by ref. 20), were individually fit into the segmented cryo-EM map of the filament with UCSF Chimera³⁹. A homology model for Arp11 was obtained with Phyre2 (ref. 40). This model could be docked with moderate confidence into the segmented EM density for Arp11 at the pointed end of dynactin. The overall shape of the model corresponded to the shape of the density for Arp11. Two copies of the prism-shaped crystal structure of p27 (PDB 3TV0) could be docked into two hollow cylindrical densities at the pointed end, thus suggesting this density to be a p25-p27 dimer. Because no homology model was available for p62, any density not attributed to Arp11 or the p25-p27 dimer was ascribed to p62. UCSF Chimera³⁹ was used to generate all surface renderings of the dynactin EM density.

DDB-MT image processing. In order to accumulate sufficient particles for 2D analysis, 24,778 micrographs of negatively stained DDB-bound MTs were collected. 30,758 MT-attached DDB particles were manually selected and extracted from the micrographs with a box size of 480 (**Supplementary Fig. 5c**). Particles were binned by a factor of 2 for processing. The signal contributed by the MT dominated the 2D reference-free alignment of the particles, thus resulting in averages of the MTs in which the DDB complex was indistinguishable. To overcome this issue, a soft-edged mask was applied to the particles such that the majority of the MT was excluded, leaving only the DDB complex and the MT surface. 2D alignment and classification of these particles revealed the overall shape of the complex, which contained an elongated region, corresponding to the dynactin and dynein tail, with circular densities closer to the MT surface, corresponding to the dynein motors. However, these averages still lacked sufficient structural detail for interpretation. With a methodology similar to that used to examine the isolated dynein dimers, we generated masks to focus on the elongated and circular regions separately; this was followed by reassembly with correlated common features. To generate the histograms of the angles between the elongated region of DDB and the MT surface (**Supplementary Fig. 5f**), we used a technique described previously⁴¹.

23. Bingham, J.B., King, S.J. & Schroer, T.A. *Methods Enzymol.* **298**, 171–184 (1998).
24. Schroer, T.A. & Sheetz, M.P. *J. Cell Biol.* **115**, 1309–1318 (1991).
25. Bertani, G. *J. Bacteriol.* **62**, 293–300 (1951).
26. Suloway, C. *et al. J. Struct. Biol.* **151**, 41–60 (2005).
27. Lander, G.C. *et al. J. Struct. Biol.* **166**, 95–102 (2009).
28. Mindell, J.A. & Grigorieff, N. *J. Struct. Biol.* **142**, 334–347 (2003).
29. Roseman, A.M. *J. Struct. Biol.* **145**, 91–99 (2004).
30. Ludtke, S.J., Baldwin, P.R. & Chiu, W. *J. Struct. Biol.* **128**, 82–97 (1999).
31. Sorzano, C.O. *et al. J. Struct. Biol.* **148**, 194–204 (2004).
32. Ogura, T., Iwasaki, K. & Sato, C. *J. Struct. Biol.* **143**, 185–200 (2003).
33. Yang, Z., Fang, J., Chittuluru, J., Asturias, F.J. & Penczek, P.A. *Structure* **20**, 237–247 (2012).
34. Tang, G. *et al. J. Struct. Biol.* **157**, 38–46 (2007).
35. Hohn, M. *et al. J. Struct. Biol.* **157**, 47–55 (2007).
36. Li, X. *et al. Nat. Methods* **10**, 584–590 (2013).
37. Scheres, S.H. *J. Struct. Biol.* **180**, 519–530 (2012).
38. Heymann, J.B. & Belnap, D.M. *J. Struct. Biol.* **157**, 3–18 (2007).
39. Goddard, T.D., Huang, C.C. & Ferrin, T.E. *J. Struct. Biol.* **157**, 281–287 (2007).
40. Kelley, L.A. & Sternberg, M.J. *Nat. Protoc.* **4**, 363–371 (2009).
41. Screpanti, E. *et al. Curr. Biol.* **21**, 391–398 (2011).